Ultrafast Carrier Dynamics and Bandgap Renormalization in Layered PtSe₂

Gaozhong Wang, Kangpeng Wang,* Niall McEvoy, Zhengyuan Bai, Conor P. Cullen, Conor N. Murphy, John B. McManus, John J. Magan, Christopher M. Smith, Georg S. Duesberg, Ido Kaminer, Jun Wang, and Werner J. Blau

Carrier interactions in 2D nanostructures are of central importance not only in condensed-matter physics but also for a wide range of optoelectronic and photonic applications. Here, new insights into the behavior of photoinduced carriers in layered platinum diselenide (PtSe₂) through ultrafast time-resolved pump–probe and nonlinear optical measurements are presented. The measurements reveal the temporal evolution of carrier relaxation, chemical potential and bandgap renormalization in PtSe₂. These results imply that few-layer PtSe₂ has a semiconductor-like carrier relaxation instead of a metal-like one. The relaxation follows a triple-exponential decay process and exhibits thickness-dependent relaxation times. This occurs along with a band-filling effect, which can be controlled based on the number of layers and may be applied in saturable absorption for generating ultrafast laser pulses. The findings may provide means to study many-body physics in 2D materials as well as potentially leading to applications in the field of optoelectronics and ultrafast photonics.

Atomically thin 2D layered crystalline materials are currently attracting much attention in the field of optoelectronics, photonics, and condensed matter physics due to their uniquely controllable properties.[1–3] By tuning the layer number and stacking sequence/angles, quantum confinement and interlayer coupling can be modified, resulting in massive changes of the electronic and optical responses of such materials. This tunability suggests that 2D layered materials are an ideal platform for developing novel devices such as spintronics[3–5] and

valleytronics,[6,7] as well as studying many-body phenomena such as charge density waves and superconductivity.[3,8,9] Among the 2D material family, platinum diselenide (PtSe₂), a noble metal dichalcogenide, has emerged as a promising material for investigating quasiparticle interactions and for developing mid-infrared devices.[10,11] The unique properties of PtSe₂ not only include a layer-dependent bandgap (bulk has zero bandgap, while mono- and bilayer have 1.2 and 0.21 eV) but also potential phase transitions from a type-II Dirac semimetal to a topological insulator or Weyl semimetal in its bulk crystalline form.[12,13] Recent studies have shown some intriguing properties of PtSe₂, such as high charge-carrier mobility,[14] intrinsic patterning,[15] piezoresistivity,[16] and spin-layer locking.[17] Moreover, PtSe₂ exhibits great potential in electronic and optoelectronic devices, for example, field effect transistors (FETs),[14,18] spintronics,[17] mid-infrared photodetectors,[10,19] gas sensors,[20] valleytronics,[12] and optical modulators.[21,22] Despite a number of reports addressing the synthesis,[11,23] electrical properties,[12,17,18] and prototype devices,[10,11,14,21] there is still a lack of understanding regarding the carrier dynamics in layered PtSe₂ on an ultrafast time scale.

Understanding ultrafast dynamical processes in 2D materials is essential for exploring many-body phenomena

Dr. G. Wang, Dr. K. Wang, Dr. Z. Bai, C. N. Murphy, Dr. J. J. Magan, C. M. Smith, Prof. W. J. Blau
School of Physics and AMBER
Trinity College Dublin
Dublin 2, Ireland
E-mail: kpwang@technion.ac.il
Dr. K. Wang, Prof. I. Kaminer
Department of Electrical Engineering and Solid-State Institute
Technion—Israel Institute of Technology
Haifa 32000, Israel
Dr. N. McEvoy, C. P. Cullen, J. B. McManus
School of Chemistry and AMBER
Trinity College Dublin
Dublin 2, Ireland

Prof. G. S. Duesberg
Institute of Physics
EIT 2
Faculty of Electrical Engineering and Information Technology
Universität der Bundeswehr München
Werner-Heisenberg-Weg 39, 85577 Neubiberg, Germany
Prof. J. Wang
Laboratory of Micro-Nano Photonic and Optoelectronic Materials and Devices
Key Laboratory of Materials for High-Power Laser
Shanghai Institute of Optics and Fine Mechanics
Chinese Academy of Sciences & CAS Center for Excellence in Ultra-intense Laser Science
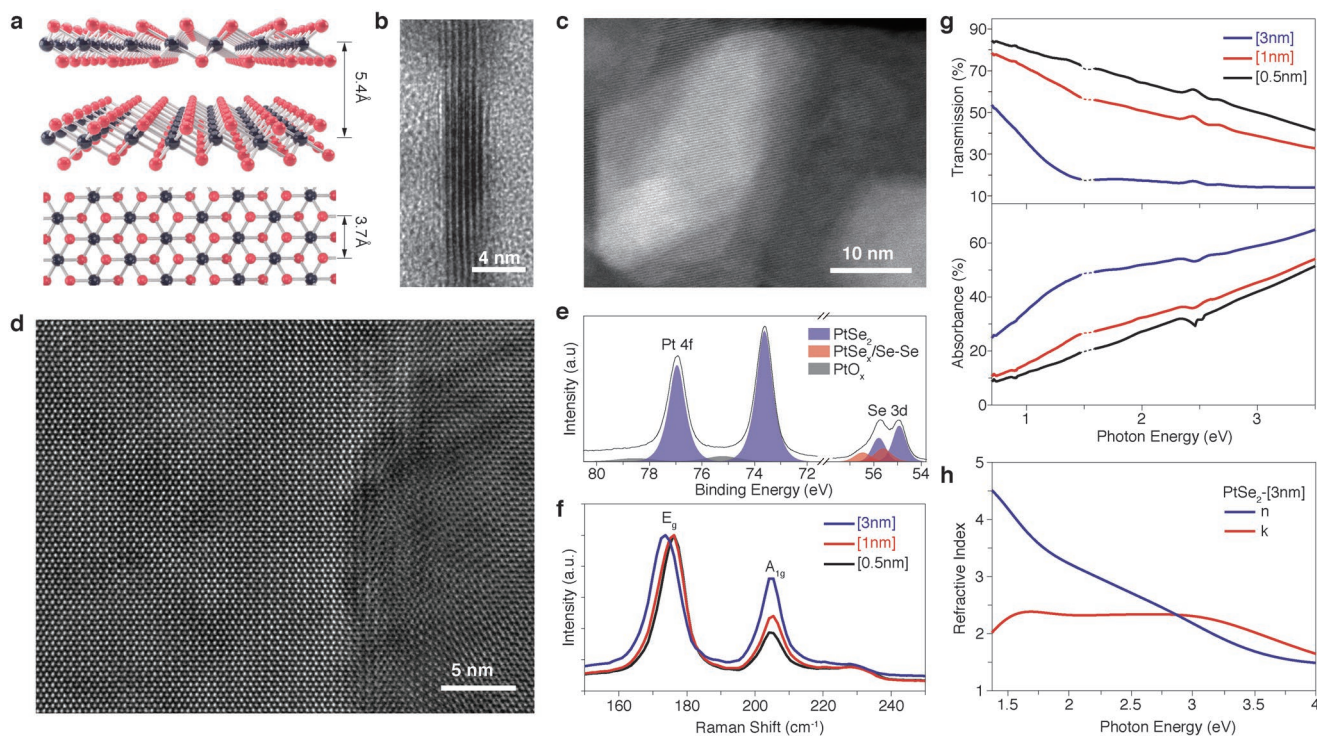Shanghai 201800, P. R. China

Figure 1. Structure and characterization of layered $PtSe_2$ films synthesized by the thermally assisted conversion method. a) Side- and top-view of 1T-type octahedral $PtSe_2$ crystal structures. Dark balls represent Pt atoms while red ones indicate Se atoms. b) TEM image of the cross-section of the $PtSe_2$ [0.5 nm] film grown on SiO_2 substrate. [0.5 nm] represents the $PtSe_2$ was selenized from an initially 0.5 nm thick Pt metallic film and so forth. The white scale bar is 4 nm. c) STEM and d) HRTEM images of the crystalline grains in a sample of 3 nm starting thickness. e) X-ray photoelectron spectroscopy of [3 nm] sample, indicating atomic percentages of Pt and Se to be about 30.3% and 69.7%, respectively. f) Raman spectra of $PtSe_2$ grown from different initial Pt thicknesses. g) Transmission and absorption spectra of the $PtSe_2$ films from visible to mid-infrared. The dashed line indicates the noise region associated with switching of photodetectors. h) Real and imaginary part of the refractive index of $PtSe_2$ from ellipsometry measurement.

and light–matter coupling from a fundamental physics point of view. Many interesting effects, such as excitonic quasiparticle interactions, hot carrier transport, Mott transition, valley selective optical Stark effect, bandgap renormalization, and charge density waves, can be probed with ultrafast carrier dynamics.[8,9,24–28] Moreover, it is possible to engineer the material's response through carrier injection by ultrafast laser pulses.[24,25,29] Thus, investigation of carrier dynamics is of importance as it provides an insight into the feasibility of utilizing the novel features of 2D systems in optoelectronic and photonic applications.

Here, we investigate the carrier dynamics of $PtSe_2$ of various thicknesses by pump–probe spectroscopy with ultrafast laser pulses. We show that separate electron and hole distributions are established within a few hundred femtoseconds after photocarrier injection, implying semiconductor- rather than metal-like carrier dynamics in semimetallic $PtSe_2$. We also observed a thickness-dependent bandgap renormalization (BGR) effect. The increased transient absorption introduced by this BGR in few-layer $PtSe_2$ can be favorable for devices requiring fast shut-off, such as high-speed optical switching and modulators. Carrier recombination was observed in a few hundred picoseconds. Additionally, our degenerate pump–probe and open-aperture z-scan measurements provide information about excited state life-times, nonlinear optical (NLO) absorption coefficients and excited-/ground-state cross-sections, which can be applicable

for most photonic devices that work with single-wavelength irradiation.

Platinum diselenide has a 1T-type layered crystal structure as presented in **Figure 1**a. As the side-view image shows, the neighboring layers are bonded by van der Waals forces with ≈5.4 Å pitch.[11] To obtain layered $PtSe_2$ thin films, we employed the method of thermally assisted conversion as previously reported[10,23] (see in the Experimental Section). In this synthesis process, a platinum film was deposited onto a fused quartz substrate and then selenized to form $PtSe_2$. During this selenization, the film thickness can expand ≈4 times comparing to that of the starting metal films.[30] According to the starting Pt metallic film thickness, we named these samples as [3], [1], and [0.5 nm]. In order to confirm the quality of the films for later measurements, we characterized them using a variety of techniques. Figure 1b shows the cross-section transmission electron microscope (TEM) image of an as-synthesized [0.5 nm] film on fused quartz, where we can count ≈6 layers in the film and a total film thickness of ≈3 nm. This ≈0.5 nm layer pitch agrees well with the experimental values reported in the literature.[10,11] In Figure 1c, a scanning transmission electron microscope (STEM) image displays the top-view geometry of a typical $PtSe_2$ crystal in [3 nm] sample, where the lattice lines are clearly seen. To confirm the 1T-type structure of our $PtSe_2$ film, we performed high-resolution transmission electron microscope (HRTEM) measurements and a typical image is shown in

**ADVANCED
SCIENCE NEWS**

www.advancedsciencenews.com

**NANO · MICRO
small**
www.small-journal.com

Figure 1d. The octahedral structure of $PtSe_2$ can clearly be seen with an average lattice constant of ≈3.8 Å, corresponding well to the reported experimental value.[11]

The chemical state and quality of the $PtSe_2$ thin film was further investigated by X-ray photoelectron spectroscopy (XPS) in Figure 1e.[11,12,18,23] The Pt 4f spectra (72–80 eV) are dominated by a doublet peak at ≈73.6 eV. This dominant Pt signal is ascribed to Pt covalently bound to Se. This peak accounts for 92% of the identified Pt, implying that the majority of the Pt has bonded to Se resulting in the formation of $PtSe_2$. A small amount of residual Pt, attributed to Pt oxides, is shown as the gray doublet at ≈75.2 eV. The Se 3d spectra are composed of two overlapping doublets, the main doublet located at 54.9 eV is attributed to $PtSe_2$ and the second, smaller doublet likely originates from undercoordinated Se, potentially from grain boundaries and edges ($PtSe_x$/Se–Se). Based on the above analysis, the atomic percentage of Pt and Se in our film contributing to $PtSe_2$ was calculated to be about 30.3% and 69.7%, respectively. Energy dispersive X-ray spectroscopy (EDS) was also carried out to study the constitution of the $PtSe_2$ films.[11] The Pt and Se EDS peaks are presented in Figure S1 in the Supporting Information. We obtained the atomic ratio of Pt/Se to be ≈30.2/69.8%, which agrees well with our XPS results. These atomic ratios of Pt/Se obtained by EDS and XPS also indicate the presence of undercoordinated Se.

We also performed Raman and UV–vis–IR spectroscopy on our $PtSe_2$ films. The obvious dependence of the position of Raman peaks on the thickness of $PtSe_2$ thin film made it possible to identify the number of layers.[14,23] In Figure 1f, the characteristic in-plane E_g mode (≈175 cm^{-1}) and out-of-plane A_{1g} mode (≈205 cm^{-1}) were observed in all three specimens.[23] As the thickness of the initial Pt thin film was increased from 0.5 to 3 nm, a slight redshift/broadening (noticeable when zoom in) in E_g peak and an increase in the relative intensity of the A_{1g} peak were observed. These results are in line with previous reports, where the A_{1g} peak intensity can be attributed to a stronger out-of-plane van der Waals interaction in samples with a greater number of layers.[23] To understand the linear optical properties of $PtSe_2$, we show the transmission and absorption of $PtSe_2$ thin films on fused quartz in Figure 1g. These measurements were carried out in an integrating sphere where the reflection and scattering were considered. As expected, thicker samples transmit less light. All $PtSe_2$ thin films exhibited broadband ground-state absorption from near-UV 354.3 nm (3.5 eV) to mid-infrared 2000 nm (0.62 eV). This broadband absorption is due to the semimetallic property of few-layered $PtSe_2$. More discussions about Raman spectroscopy and linear optical absorption of $PtSe_2$ can be seen in our previous works.[16]

The complex refractive index is a fundamental property of a material that not only determines its optical responses, but also directly connects to its complex permittivity and dielectric constant. We determined the real and imaginary part of the refractive index n and k (the latter also known as the extinction coefficient) of the $PtSe_2$ [3 nm] sample by spectroscopic ellipsometry in the wavelength range from 200 to 900 nm (see in the Experimental Section). The resulting refractive index and extinction coefficient are presented in Figure 1h. The real refractive index increased from 1.5 to 4.5 as the photon energy changed from 4 to 1.38 eV, while the extinction coefficient is relatively flat around 2.4. This refractive index is important for analyzing our transient spectroscopy results in later sections.

The excited-carrier dynamics of layered $PtSe_2$ films were investigated using time-resolved spectroscopy with 400 nm (3.1 eV) femtosecond laser pulses. By employing near-UV high-energy photons for excitation, optically induced structural changes, that may happen with ultrafast IR pulse excitation, can be minimized thus allowing a straightforward detection of electronic responses.[31,32] Since the bandgap of $PtSe_2$ is smaller than the pump photon energy,[12] the 400 nm photons can effectively excite the electrons from the valence to conduction band. The fluence of the 3.1 eV pump pulse was fixed at 0.90 mJ cm^{-2} for [0.5], [1], and [3 nm] samples, corresponding to excitation densities of 0.79×10^{15}, 0.85×10^{15}, and 1.09×10^{15} cm^{-2}. By probing with white light from 1.72 eV (720 nm) to 2.64 eV (470 nm), mapping of the optical differential transmission (DT) as a function of delay time was obtained, as shown in **Figure 2**a–c. Here, $\Delta T/T = (T-T_0)/T_0$, where T_0 is the linear optical transmission. Deep colored areas (0–1 ps) near zero delay time across all probing wavelengths reflect positive DT signals in all three samples. These positive signals are due to the filling of states and Pauli-blocking by optically excited carriers.[29] Negative DT signals were found around 2–4 ps, which are more evident in Figure 2d–i. This negative DT signal can be attributed to BGR caused by the filling of a large amount of electron–hole plasma as shown schematically in **Figure 3**a. This BGR can result in a redshift in interband absorption and less transmission.[29,33,34] Modification of structural dynamics resulting in bandgap shrinkage has been demonstrated for graphite.[31,32] This structural effect was induced by coupling between photoexcited carriers and optical photons generated by infrared laser pulses. Electronic excitations can be decoupled from the structural effect by pumping with near-UV photons,[32] such as in the case of our transient spectroscopy in Figure 2. Therefore, the dynamics of BGR we observed in Figures 2 and 3 are more likely to originate from electron–electron interactions than a structural effect. To study the electron–hole recombination kinetics in $PtSe_2$, we performed a scan of the DT with long delay time (to 100 ps) and the results are presented in Figure S2 in the Supporting Information.

To obtain carrier relaxation times from experimental results, we analyzed the DT spectrum along the temporal axis by employing a triple-phase decay equation, which has taken into account the convolution of the pump and probe pulses (see Section 3 in the Supporting Information). As shown in Figure 2 and Figure S2 in the Supporting Information, this triple-phase model provides satisfying fitting results (solid lines). To provide a general idea about the relaxation times in $PtSe_2$, we summarize the time constants obtained from the integrated spectra (Figure 2g–i) in Table S1 in the Supporting Information.

In a pump–probe experiment, carriers generally experience initial excitation, rapid thermalization, cooling, and recombination. The optical pulses excite a large number of carriers into a nonequilibrium distribution at time-zero. This nonthermal regime cannot be described by any thermal distribution, e.g., Maxwell–Boltzmann or Fermi–Dirac (FD) functions.[29] The carriers then dephase to a quasiequilibrium thermal regime via carrier–carrier scattering and/or emission of phonons in a
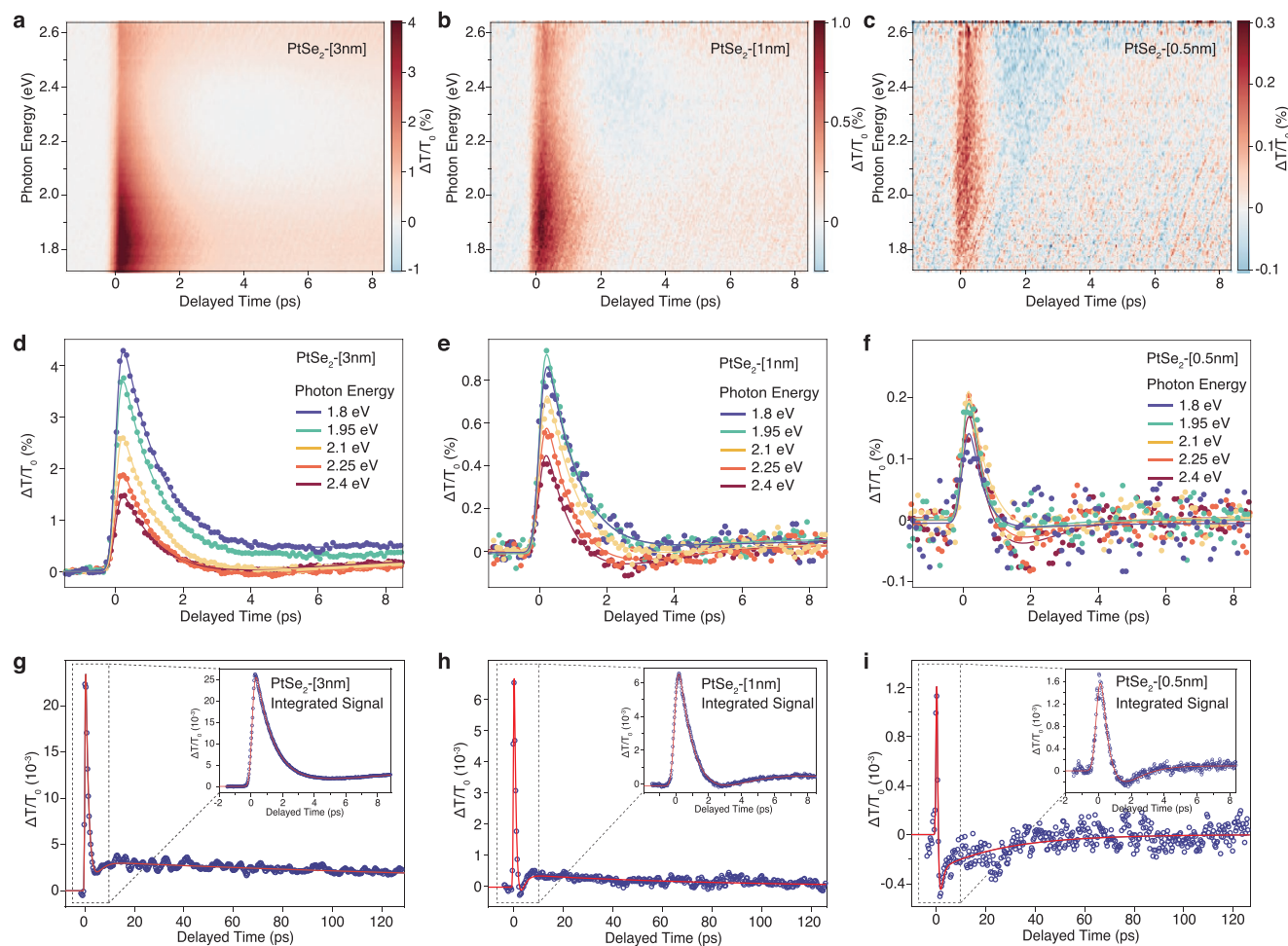
**ADVANCED
SCIENCE NEWS**

www.advancedsciencenews.com

NANO · MICRO

small

www.small-journal.com

Figure 2. Time- and spectrally resolved differential transmission (DT) of layered PtSe$_2$ nanostructures with 3.1 eV (400 nm) pump pulses, showing the carrier dynamics varying as a function of probe photon frequency and thickness and giving evidence of the bandgap renormalization. a–c) Time-resolved DT mapping in the visible range from 1.72 eV (720 nm) to 2.64 eV (470 nm) for the PtSe$_2$ samples with 3, 1, and 0.5 nm starting Pt thickness. The pump fluence was 0.94 mJ cm^{-2} for all three PtSe$_2$ samples. d–f) Transient DT for 2.6, 2.0, and 1.80 eV photons in (a–c). Solid lines are the fitting results determined by Equation (S1) in the Supporting Information with a nonlinear regression algorithm. The differences of DT between probe photon energies show the dynamics of the carrier that will be discussed in Figure 3. g–i) Spectrally integrated DT between all the probe wavelengths, showing a triple-phase carrier relaxation including carrier–photon scattering, bandgap renormalization, and electron–hole recombination.

few tens of femtoseconds, which is beyond our temporal resolution. These carriers are subsequently cooled via intraband scattering paths. The lifetimes of this intraband scattering in Figure 2g–i are calculated to be 0.65, 1.09, and 1.71 ps for PtSe$_2$ sample with [0.5], [1], and [3 nm] starting thickness. The state filling by a large amount of electron–hole pairs introduces the shrinkage of the bandgap, i.e., band renormalization, leading to the negative signal in Figure 2. The time constants related to this BGR are measured to be 0.91, 1.3, and 1.8 ps for [0.5], [1], and [3 nm] samples. The electrons in the lower excited states finally recombine with corresponding holes via the assistance of trap states (Shockley–Read–Hall recombination). These trap states may originate from excess Se atoms in the samples implied by the XPS and EDS results in Figure 1e and Figure S1 in the Supporting Information, respectively. The recombination time constants correspond to 27.3, 80.7, and 256.5 ps for [0.5], [1], and [3 nm] PtSe$_2$ thin films, respectively, as seen in Table S1 in the Supporting Information, showing a dramatic increase

with increasing film thickness. This difference in recombination rate may be attributed to a variable defect density, where more defects are present in thinner films because of unreacted selenium and/or surface states.

We applied a quasiequilibrium carrier distribution model to quantify the contribution of BGR dE, carrier temperature T_c, chemical potential μ.[33] The changes of the imaginary part of permittivity after optical excitation are

$$\Delta\epsilon'' = \epsilon''(E+dE) - \epsilon''(E) - 2\epsilon''(E+dE) f\left(\frac{E+dE}{2}, T_c\right) \quad (1)$$

where ϵ'' is the imaginary part of the complex permittivity ϵ at photon energy E. The complex permittivity $\underline{\epsilon} = \epsilon' - i\epsilon''$ is connected to the complex refractive index n by relationship $\underline{\epsilon} = \underline{n}^2 = (n - ik)^2$, where n and k can be interpolated from the complex refractive index measurement in Figure 1h. dE is the bandgap shift from BGR. For simplicity, we evaluated the
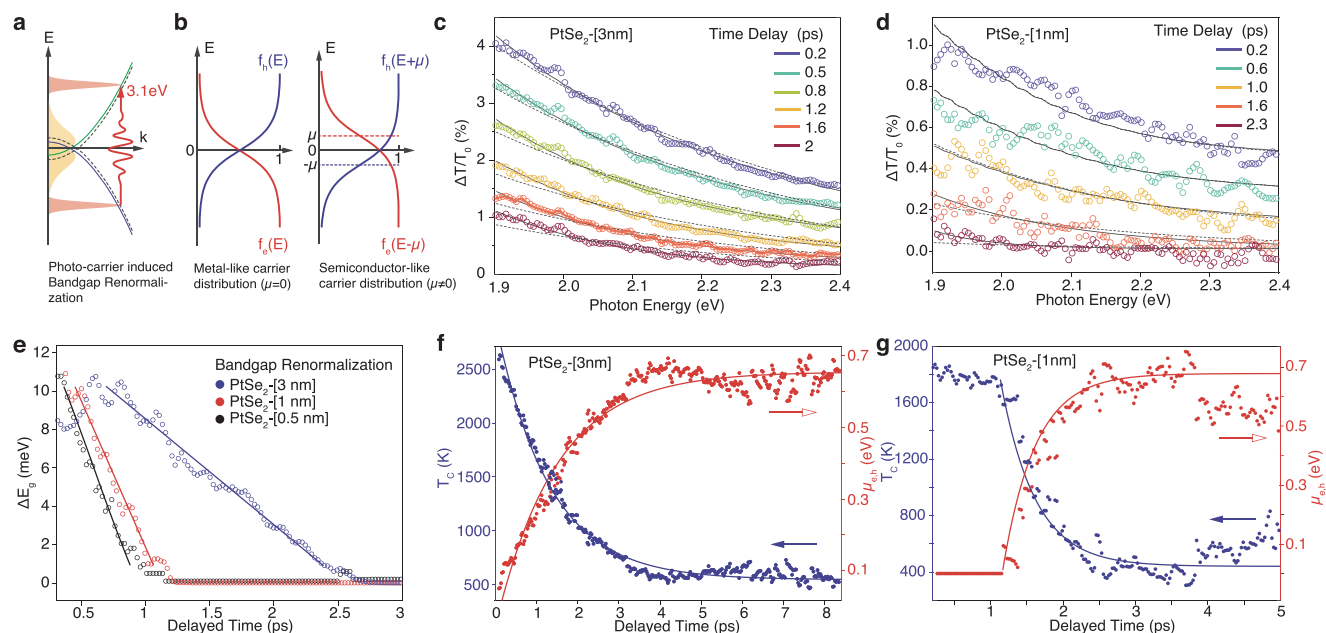
Figure 3. Analysis of differential transmission (DT) spectra employing the quasiequilibrium model described in Equation (1) in the Supporting Information, indicating the semiconductor-like carrier dynamics in few-layer PtSe$_2$. a) Schematic of the shrunken energy bands (solid lines) from original ones (dashed lines) of dE due to bandgap renormalization (BGR). Nonthermal photocarriers (red) are first introduced by ultrafast laser pulses, then cooled to thermal electron–hole plasma (yellow) that induces BGR. b) Illustrations show the metal- (zero chemical potential) and semiconductor-like carrier distributions (nonzero chemical potential) in the thermal region after optical excitation. c,d) Circles: DT spectra of PtSe$_2$ for fixed delay time from 0.2 to 2 ps. Solid lines: best fit spectra by treating carrier temperature, amplitude of BGR, and chemical potential as free parameters ($\mu \neq 0$). Dash lines: best fit spectra with the same model as solid lines but assuming zero chemical potential ($\mu = 0$). e) Circles: time-dependent band shift introduced by BGR in optically excited PtSe$_2$ samples derived from fits in (c,d) and Figure S3 in the Supporting Information. Solid lines are for visual guide. f,g) Circles: carrier temperature T_c and chemical potential μ as a function of delay time obtained from fits in (c,d). Lines: exponential fitting for visual guide.

average behavior of electrons and holes and assumed that they behave equivalently, so the Fermi–Dirac distribution of carriers becomes $f(E, T_c) = (1 + \exp[(E - \mu)/T_c])^{-1}$. We specified two situations for chemical potential ($\mu \neq 0$ and $\mu = 0$) because they correspond to different hot-carrier equilibration processes after optical excitation as Figure 3b shows. For $\mu \neq 0$, the electrons and holes establish a separate FD distribution in the conduction and valence bands if the intraband carrier scattering is much faster than the interband one. For $\mu = 0$, in contrast, the interband and intraband scattering rate are similar, leading to a distribution that can be described by a single FD distribution.[29,33] Thus, by fitting for both cases, it is possible to ascertain which type of carrier dynamics dominates in layered PtSe$_2$.

To accurately calculate the variation in DT, changes of the PtSe$_2$ surface reflection and the effect from the fused quartz substrate should be also taken into account. To this end, a characteristic matrix method was employed to calculate the total transmission T for our PtSe$_2$ sample on fused quartz (see Section 4 in the Supporting Information). Figure 3c,d displays fits to the DT spectra by nonlinear regression using Equation (1) and Equations (S2) and (S3) in the Supporting Information. For DT spectra of PtSe$_2$ [3 nm] in Figure 3c, fits to the experimental results using separate FD distributions $\mu \neq 0$ (solid line) are much better than those using a single FD distribution $\mu = 0$ (dash line) for all delay times. This phenomenon implies that, like graphite, the carrier dynamics of PtSe$_2$ [3 nm] is more similar to that of a semiconductor than that of a metal.[29,33] For DT spectra of PtSe$_2$ [1 nm] in Figure 3d, both distributions

($\mu \neq 0$ and $\mu = 0$) show indistinguishable behavior for 0.2 and 0.6 ps delay time. For a delay time above 1 ps, however, the fitting using $\mu \neq 0$ is still better than for $\mu = 0$. More details about the chemical potential as a function of delay time can be found in Figure 3f,g. The time-dependent BGR for both samples, dE, can be found in Figure 3e. The BGR in PtSe$_2$ has a similar starting value of ≈10 meV at the first picosecond after the carrier injection for all PtSe$_2$ films, while the thicker ones show a slower relaxation. The BGR almost fully decays after ≈2.6, ≈1.2, and ≈1 ps for the [3], [1], and [0.5 nm] samples, respectively. The carrier temperature of PtSe$_2$ samples are also extracted from the fits as seen in Figure 3f,g, nicely showing carrier cooling. In PtSe$_2$ [3 nm], carriers cooled from about 2500 to 500 K over 4 ps nearly exponentially. However, in PtSe$_2$ [1 nm] the carrier temperature appears to linearly decrease from 1850 to 1750 K in the first picosecond, and then exponentially cools to ≈400 K after 2.5 ps. The fitted chemical potentials in Figure 3f,g also show similar behavior with temperature. These differences in temperature and chemical potential may be due to the fact that the carrier intraband equilibrium after optical interband excitation in PtSe$_2$ [1 nm] is much slower than that in PtSe$_2$ [3 nm], where the latter looks "instantaneous" because of our ≈200 fs temporal resolution.

From the DT spectra of PtSe$_2$, we observed obvious optically induced bleaching with photon energy from 1.72 eV (720 nm) to 2.64 eV (470 nm) due to band filling. This effect implies a saturable absorption response in PtSe$_2$, which is important for broad applications working at a single wavelength,
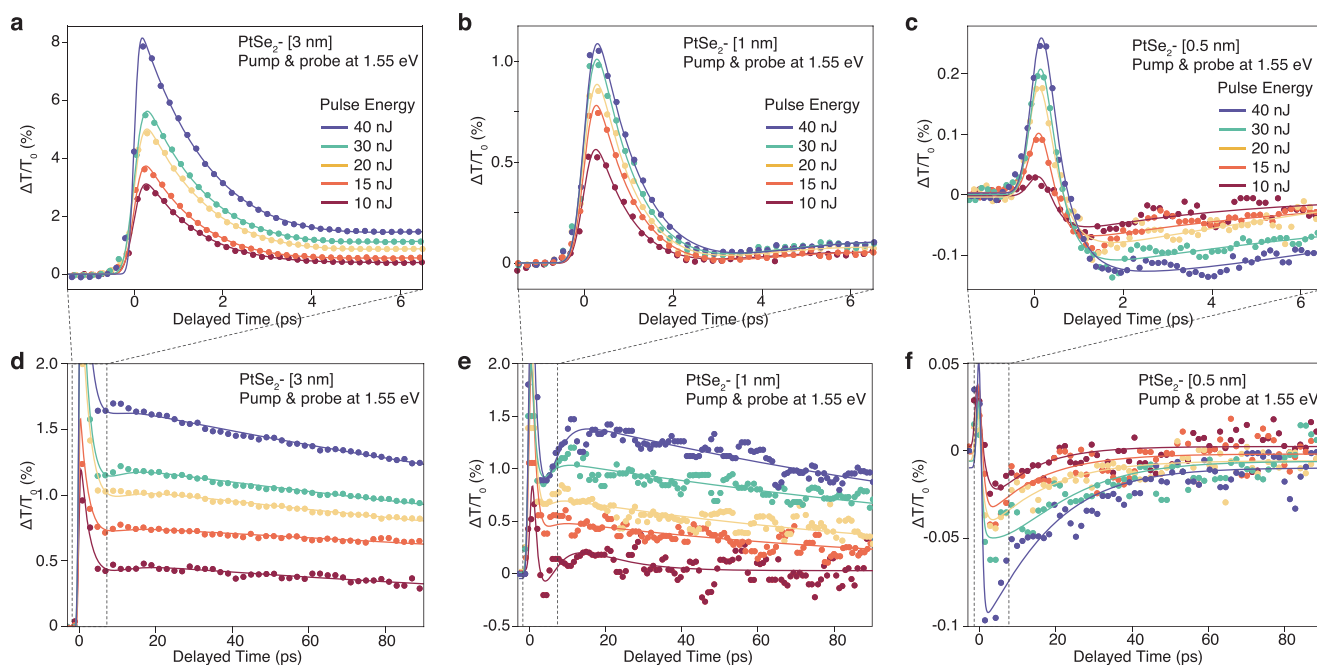
Figure 4. Degenerate pump–probe measurements, revealing the carrier-dynamics and the nonlinear absorption under pump and probe irradiation at the same wavelength. a–c) Time-resolved DT spectra of layered PtSe$_2$ samples with 1.55 eV (800 nm) pump and probe pulses. Experimental results are shown by solid circles and the lines are fitted curves using a triple-exponential model. Every 10 nJ laser pulse energy corresponds to 0.40 mJ cm^{-2} pump fluence here. The polarizations of pump and probe pulses are orthogonal to each other. d–f) are the same measurements as (a–c) but showing the carrier relaxations over a longer time scale. The time constants of the fittings are summarized in Table S2 in the Supporting Information.

such as optical-switching and mode-locking. Thus degenerate pump–probe experiments, where the pump and probe pulses have the same wavelength, is both an effective and appropriate technique to reveal the carrier dynamics of ground and excited states for such applications. We carried out degenerate pump–probe experiments at 800 nm for the three samples with pump fluence from 10 to 40 nJ (see **Figure 4**). Every 10 nJ corresponds to an excitation density of 7.90×10^{14}, 4.37×10^{14}, and 3.23×10^{14} cm^{-2} for [3], [1], and [0.5 nm] starting Pt thickness, respectively. The measurements in Figure 4a–c range from −1.8 to 6.5 ps, showing details of electron states near time-zero and longer delay times in Figure 4d–f corresponding to carrier recombination.

Positive DT signals were observed in all the three PtSe$_2$ samples immediately after excitation, which were attributed to the photoinduced bleaching that is caused by Pauli-blocking.[29] Upon irradiation by the pump, electrons are promoted from the ground to excited states. This band filling will reduce the probability of absorption of probe photons and results in positive changes in DT $\Delta T/T_0$ as seen in Figure 4a–c. Then the electron/holes cooled to thermal regime via carrier–phonon scattering, exhibiting a decrease in DT. After around 2 ps, $\Delta T/T_0$ was observed to increase slightly for all samples, similar to the DT spectra in Figure 2. Turning points are more obvious in Figure 4d–f, where there appears to be dips resulting in negative DT in [1] and [0.5 nm] samples. These negative DT signals in Figure 4 may be contributed to by two mechanisms: 1) structural changes induced by coupling of the excited carriers to coherent phonons taking place in hundreds of fs because of the infrared pump (800 nm) pulses;[31,32] or 2) red shifting of

interband absorption from BGR.[29,33] Further studies using fs-electron energy loss spectroscopy (FEELS) could help to clarify such processes.[31,32] After ≈10 ps, electron–hole recombination dominates the optical response for all samples and the details are shown in Figure 4d–f. The time constants related to the above carrier relaxations were also obtained by fitting with the triple-phase decay model Equation (S1) in the Supporting Information. We determined the decay times of carrier–phonon scattering τ_c to be 0.52, 0.9, and 1.29 ps for [0.5], [1], and [3 nm] samples, respectively, and that of the negative signal τ_N to be 1.54, 1.73, and 2.63 ps. The electron–hole recombination times τ_r are in the range of 81.2–316.4 ps (see Table S2 in the Supporting Information). These decay times are approximately equal to those in Table S1 in the Supporting Information which we obtained from transient absorption spectroscopy and also imply that carrier relaxation is faster in thinner samples.

To further study the band-filling effect and obtain potentially thickness-dependent NLO coefficients for PtSe$_2$, we performed a series of open-aperture z-scan measurements using a single femtosecond laser beam. These measurements were based on 800 nm pulses laser with an ≈100 fs pulse duration at room temperature. In the open-aperture z-scan measurement, the sample transmission is recorded as a function of its position along the focused laser beam propagation direction (z-axis). **Figure 5**a–c presents z-scan results for the three PtSe$_2$ samples at 800 nm, where the normalized transmission increases when the sample moves toward the focused point (z = 0) and peaks at z = 0. This is saying the optical transmission of PtSe$_2$ increases with the laser irradiance intensity. Such response is known as saturable absorption, which is caused by Pauli-blocking. Under
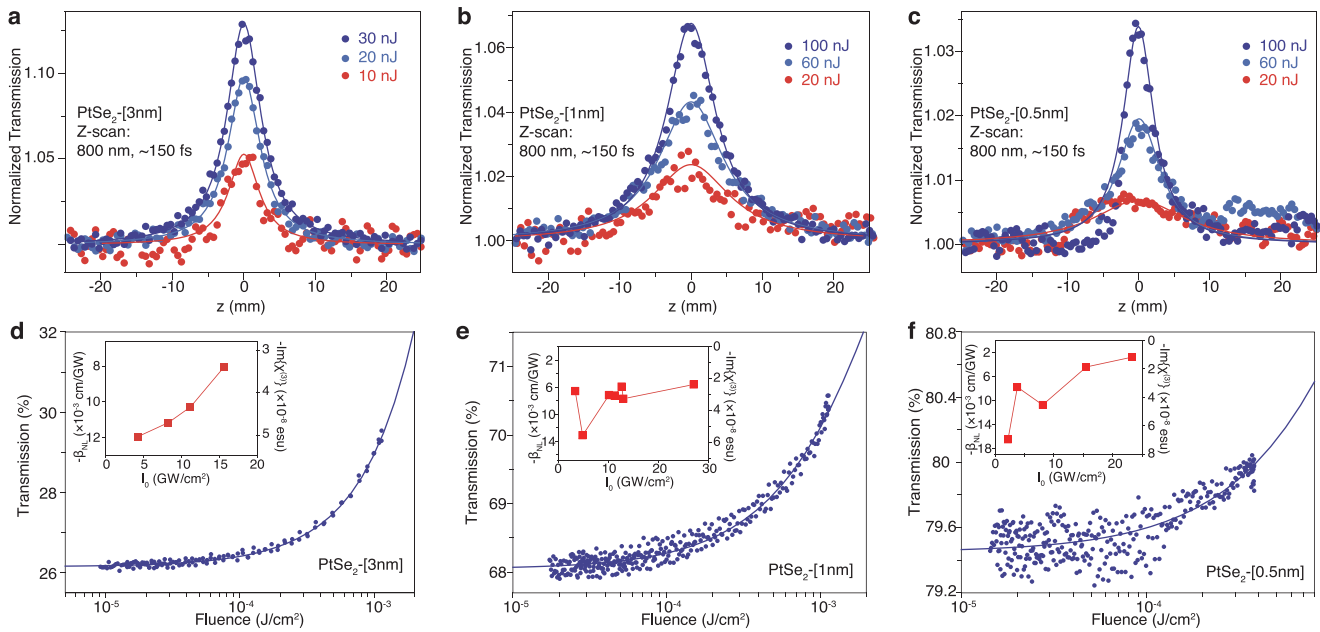
ADVANCED
SCIENCE NEWS
www.advancedsciencenews.com

NANO · MICRO
small
www.small-journal.com

Figure 5. Nonlinear optical response of PtSe$_2$ thin films from z-scan, showing saturable absorption, i.e., transmission increases with the incident intensity. a–c) Open-aperture z-scan traces using 800 nm femtosecond laser pulses. d–f) Transmission as a function of laser fluence for PtSe$_2$ samples obtained from the fittings employing the modified Frantz–Nodvik equation. Insets: nonlinear absorption coefficient β_{NL} and imaginary part of the third-order NLO susceptibility Im$\{\chi^{(3)}\}$ versus on-focused intensity I_0.

intense laser irradiation, electrons are pumped to fill the excited states and the excited state cannot accept more incoming electrons because of the Pauli-exclusion principle. This allows the majority of intense light to pass through and blocks the light with low intensity. This photoinduced response of PtSe$_2$ can be exploited as a saturable absorber for passive mode-locking to generate femtosecond laser pulses, especially in mid-infrared range because of its small bandgap.[21,22,35]

The NLO coefficients from z-scan traces were obtained from the standard z-scan model, i.e., $T_{norm}(z) = \ln(1 + q_0)/q_0$, where $q_0 = \beta_{NL}I_0L_{eff}$ and effective length $L_{eff} = [1 - \exp(-\alpha_0 L)]/\alpha_0$.[36] The saturation intensity I_s was fitted by solving the light propagation equation in saturable absorber, i.e., $dI/dz = -\alpha_0 I/(1 + I/I_s)$. The fitted curves are presented as solid lines in Figure 5, showing excellent agreement with the experimental results. The corresponding NLO coefficients are summarized in Table S3 in the Supporting Information. We calculated the imaginary part of the third-order optical susceptibility using Im$\{\chi^{(3)}\} = (10^{-7}c\lambda n^2)/(96\ \pi^2)\beta_{NL}$ (esu), in which c is the speed of light, λ is the laser wavelength, and n is the real part of refractive index. Determining the excited-state and ground-state cross-sections of PtSe$_2$ is crucial to designing effective photonic devices. To obtain both cross-sections, we employed the modified Frantz–Nodvik equation[37]

$$T(F) = T_0 + \frac{T_{FN} - T_0}{1 - T_0}(T_{max} - T_0) \tag{2}$$

where $T_0 = \exp(-\sigma_g k)$ is the linear transmission and $T_{max} = \exp(-\sigma_e k)$ is the maximum transmission at relative high intensity. $T_{FN} = \ln\left[1 + T_0\left(e^{\frac{\sigma_g F}{\hbar\omega}} - 1\right)\right]/(\sigma_g F/\hbar\omega)$. σ_e and σ_g are the excited-state and ground-state cross-section, and F is the laser-pulse fluence. $k = NL$ is the absorber density per unit area, in

which N is the atom density of the absorber and L is the optical path inside the sample.

The fitting results based on Equation (2) were plotted in Figure 5d–f and the fitted parameters are listed in Table S3 in the Supporting Information. We obtained a saturated intensity of 75.0, 92.3, and 187.5 GW cm^{-2} for [3], [1], and [0.5 nm] samples respectively, implying easier saturation for thicker samples. The imaginary part of the third-order NLO susceptibility for the PtSe$_2$ thin films is on the order of -10^{-8} esu, which is ≈10 times larger than that (-10^{-9} esu) of few-layer MoSe$_2$ and WS$_2$ saturable absorbers.[38] The modulation depth of the film was observed to be dependent on thickness with corresponding values of 25.61%, 8.04%, and 4.25% for [3], [1], and [0.5 nm] films, respectively. The absorption cross-sections of the ground state for the three films are calculated to be 2.25×10^{-16}, 2.08×10^{-16}, and 1.87×10^{-16} cm^2, while those of the excited states are found to be 1.74×10^{-16}, 1.47×10^{-16}, and 0.92×10^{-16} cm^2, respectively, showing a decrease with increasing thickness (see Table S3 in the Supporting Information). This implies that nonlinear absorption in PtSe$_2$, such as modulation depth, can be tuned by modifying the film thickness, offering a degree of flexibility in designing saturable absorbers.

In summary, ultrafast bandgap renormalization, carrier dynamics, and Pauli-blocking induced saturable absorption were observed in layered PtSe$_2$ thin films with transient absorptive spectroscopy, degenerate pump–probe spectroscopy, and open-aperture z-scan measurements. The relaxation of excited carriers follows a triple exponential decay with thickness-dependent characteristic times of ≈0.6–1.7, ≈2-3, and ≈27–250 ps, which originate from carrier–phonon scattering, bandgap renormalization and electron–hole recombination, respectively. The analysis of the chemical potential evolution

strongly implies that carrier dynamics in few-layered PtSe$_2$ follow semiconducting behavior instead of metallic behavior. The amplitude of bandgap renormalization is estimated to be $\approx$10 meV. Pauli-blocking of electrons in excited states leads to a band-filling effect, i.e., saturable absorption, with increasing NLO modulation depth as the number of layers increases. Strong thickness-dependent saturation intensities of 75.0, 92.3, and 187.5 GW cm^{-2} were measured for the [3], [1], and [0.5 nm] films, respectively. The results will benefit the development of novel optoelectronic devices based on layered PtSe$_2$, particularly for mid-infrared optical modulators and photodetectors, and give a view toward potential applications in monowavelength photonic devices.

Experimental Section

Materials: PtSe$_2$ films were synthesized by thermally assisted conversion of platinum films as previously reported.[10,11] Briefly, platinum was deposited onto fused quartz substrates via sputtering using a Gatan precision etching and coating system. A quartz-crystal microbalance was used to monitor the deposition process. The Pt-deposited substrates were then placed in a quartz-tube vacuum furnace and heated up to 450 °C. Se powder was heated to 220 °C in an independently controlled heating zone upstream of the Pt samples and its vapor was carried to the Pt films under a 150 sccm flow of forming gas (10% H$_2$/Ar). A dwell time of 2 h was used for complete selenization.

Characterizations: The TEM specimens were prepared by transferring the PtSe$_2$ film onto a holey-carbon TEM grid. The PtSe$_2$ film used was grown on a SiO$_2$ coated silicon wafer under the same conditions as other samples. Then, the SiO$_2$ layer was etched away by floating the sample on 2 M NaOH solution. After etching the substrate, the PtSe$_2$ film remained floating on the surface. The PtSe$_2$ film was then transferred to deionized water and then fished onto a holey-carbon TEM grid and dried before TEM measurements. The lamella for cross-section TEM imaging was prepared by the standard technique with focused ion beam. More morphological information and thickness of the Pt and converted PtSe$_2$ films can be found in the previous reports.[20,30]

A confocal Raman spectrometer (Witec Alpha 300 R, 1800 lines mm^{-1} spectral grating) was employed to characterize the thin films with 532 nm excitation wavelength. To measure absorption and reflection in the UV–vis–NIR range, a spectrophotometer (Perkin Elmer Lambda 1050) equipped with an integrating sphere was used.

Ellipsometry: The complex refractive index of the PtSe$_2$ thin films was measured on a SOPRA GESP5 rotating polarizer Spectroscopic ellipsometer. Spectra were taken from 200 to 900 nm at a resolution of 5 nm and under multiple angles of incidence of 72°, 75°, and 78° for each sample. The data was then fitted using a dispersion law model based on four Lorentzian oscillators.

Transient Spectroscopy: The 800 nm pulses with an $\approx$100 fs pulse width were generated by a mode-locked Ti:sapphire laser (Coherent RegA 9000, repetition rate 100 kHz). Then, the beam was split into two such that one beam went into a beta barium borate (BBO) crystal to generate 400 nm femtosecond pulses for pumping. This pump beam was then modulated by an optical chopper. The other beam was focused onto a 3 mm thick sapphire to obtain a supercontinuum white light source for probing. These pulses were then filtered by a 750 nm short-pass ($\approx$480–750 nm) filter to remove 800 nm fundamental wavelength and then delayed by a motorized stage. Both pump and probe were combined collinearly by a dichroic mirror (450 nm) and focused onto the samples by an $f = 10$ cm convex lens with the same polarization. The 400 nm pump was then blocked by a 425 nm long-pass filter. The transmitted light was collected by a charge-coupled device (CCD) spectrometer and then the differential transmission signals at the frequency of the optical chopper were extracted via a home-developed computer program.

Degenerate Pump–Probe: Femtosecond 800 nm pulses were split into two beams for pump and probe. The probe pulses were delayed by a motorized stage and their polarization was rotated by 90° with respect to the pump pulses to eliminate coherent artefacts. The pump and probe beams were modulated by a chopper at different frequencies. Then, both beams were noncollinearly combined and focused on the samples. The light transmitted through the sample was filtered by a polarizer to block the pump beam. The final signal was detected by a single Si photodiode and collected with a lock-in amplifier (Signal Recovery, SR7270) locked at 1157 Hz, the sum frequency of pump and probe beams.

Z-Scan: An open-aperture z-scan setup was then employed for nonlinear optical absorption measurements. Two beams were split from the 800 nm femtosecond laser and chopped at different frequencies. One was used as reference while the other was focused onto the sample to give signals. Both beams were reflected into a single Si photodiode and the reference and sample signals were picked up by a dual-reference lock-in amplifier. The sample position along the z-axis was controlled by a motorized linear stage. The linear absorption coefficient α_0 was determined to be 8.26 × 10^5 cm^{-1} from the sample of 0.5 nm starting thickness based on the relationship $T_0 = \exp(-\alpha_0 L)$. According to the Beer–Lambert law, the thicknesses of PtSe$_2$ thin films for [0.5], [1], and [3 nm] samples were obtained to be $\approx$3.0, $\approx$4.6, and $\approx$16.2 nm.

Supporting Information

Supporting Information is available from the Wiley Online Library or from the author.

Conflict of Interest

The authors declare no conflict of interest.

[1] K. Novoselov, A. Mishchenko, A. Carvalho, A. C. Neto, *Science* **2016**, *353*, aac9439.
[2] A. K. Geim, *Science* **2009**, *324*, 1530.

[3] Q. H. Wang, K. Kalantar-Zadeh, A. Kis, J. N. Coleman, M. S. Strano, *Nat. Nanotechnol.* **2012**, *7*, 699.

[4] D. Xiao, G.-B. Liu, W. Feng, X. Xu, W. Yao, *Phys. Rev. Lett.* **2012**, *108*, 196802.

[5] D. Pesin, A. H. MacDonald, *Nat. Mater.* **2012**, *11*, 409.

[6] K. F. Mak, K. He, J. Shan, T. F. Heinz, *Nat. Nanotechnol.* **2012**, *7*, 494.

[7] E. J. Sie, J. W. McIver, Y.-H. Lee, L. Fu, J. Kong, N. Gedik, *Nat. Mater.* **2015**, *14*, 290.

[8] A. Zong, A. Kogar, Y.-Q. Bie, T. Rohwer, C. Lee, E. Baldini, E. Ergeçen, M. B. Yilmaz, B. Freelon, E. J. Sie, H. Zhou, J. Straquadine, P. Walmsley, P. E. Dolgirev, A. V. Rozhkov, I. R. Fisher, P. Jarillo-Herrero, B. V. Fine, N. Gedik, *Nat. Phys.* **2019**, *15*, 27.

[9] B. Sipos, A. F. Kusmartseva, A. Akrap, H. Berger, L. Forró, E. Tutiš, *Nat. Mater.* **2008**, *7*, 960.

[10] C. Yim, N. McEvoy, S. Riazimehr, D. S. Schneider, F. Gity, S. Monaghan, P. K. Hurley, M. C. Lemme, G. S. Duesberg, *Nano Lett.* **2018**, *18*, 1794.

[11] X. Yu, P. Yu, D. Wu, B. Singh, Q. Zeng, H. Lin, W. Zhou, J. Lin, K. Suenaga, Z. Liu, Q. J. Wang, *Nat. Commun.* **2018**, *9*, 1545.

[12] Y. Wang, L. Li, W. Yao, S. Song, J. T. Sun, J. Pan, X. Ren, C. Li, E. Okunishi, Y.-Q. Wang, E. Wang, Y. Shao, Y. Y. Zhang, H. Yang, E. F. Schwier, H. Iwasawa, K. Shimada, M. Taniguchi, Z. Cheng, S. Zhou, S. Du, S. J. Pennycook, S. T. Pantelides, H.-J. Gao, *Nano Lett.* **2015**, *15*, 4013.

[13] K. Zhang, M. Yan, H. Zhang, H. Huang, M. Arita, Z. Sun, W. Duan, Y. Wu, S. Zhou, *Phys. Rev. B* **2017**, *96*, 125102.

[14] Y. Zhao, J. Qiao, Z. Yu, P. Yu, K. Xu, S. P. Lau, W. Zhou, Z. Liu, X. Wang, W. Ji, Y. Chai, *Adv. Mater.* **2017**, *29*, 1604230.

[15] X. Lin, J. C. Lu, Y. Shao, Y. Y. Zhang, X. Wu, J. B. Pan, L. Gao, S. Y. Zhu, K. Qian, Y. F. Zhang, D. L. Bao, L. F. Li, Y. Q. Wang, Z. L. Liu, J. T. Sun, T. Lei, C. Liu, J. O. Wang, K. Ibrahim, D. N. Leonard, W. Zhou, H. M. Guo, Y. L. Wang, S. X. Du, S. T. Pantelides, H. J. Gao, *Nat. Mater.* **2017**, *16*, 717.

[16] S. Wagner, C. Yim, N. McEvoy, S. Kataria, V. Yokaribas, A. Kuc, S. Pindl, C.-P. Fritzen, T. Heine, G. S. Duesberg, M. C. Lemme, *Nano Lett.* **2018**, *18*, 3738.

[17] W. Yao, E. Wang, H. Huang, K. Deng, M. Yan, K. Zhang, K. Miyamoto, T. Okuda, L. Li, Y. Wang, H. Gao, C. Liu, W. Duan, S. Zhou, *Nat. Commun.* **2017**, *8*, 14216.

[18] Z. Wang, Q. Li, F. Besenbacher, M. Dong, *Adv. Mater.* **2016**, *28*, 10224.

[19] L.-H. Zeng, S.-H. Lin, Z.-J. Li, Z.-X. Zhang, T.-F. Zhang, C. Xie, C.-H. Mak, Y. Chai, S. P. Lau, L.-B. Luo, Y. H. Tsang, *Adv. Funct. Mater.* **2018**, *28*, 1705970.

[20] C. Yim, K. Lee, N. McEvoy, M. O'Brien, S. Riazimehr, N. C. Berner, C. P. Cullen, J. Kotakoski, J. C. Meyer, M. C. Lemme, G. S. Duesberg, *ACS Nano* **2016**, *10*, 9550.

[21] J. Yuan, H. Mu, L. Li, Y. Chen, W. Yu, K. Zhang, B. Sun, S. Lin, S. Li, Q. Bao, *ACS Appl. Mater. Interfaces* **2018**, *10*, 21534.

[22] L. Tao, X. Huang, J. He, Y. Lou, L. Zeng, Y. Li, H. Long, J. Li, L. Zhang, Y. H. Tsang, *Photonics Res.* **2018**, *6*, 750.

[23] M. O'Brien, N. McEvoy, C. Motta, J.-Y. Zheng, N. Berner, J. Kotakoski, K. Elibol, T. Pennycook, J. Meyer, C. Yim, M. Abid, T. Hallam, J. Donegan, S. Sanvito, D. Georg, *2D Mater.* **2016**, *3*, 021004.

[24] Z. Ye, D. Sun, T. F. Heinz, *Nat. Phys.* **2017**, *13*, 26.

[25] A. Chernikov, C. Ruppert, H. M. Hill, A. F. Rigosi, T. F. Heinz, *Nat. Photonics* **2015**, *9*, 466.

[26] Z. Guo, Y. Wan, M. Yang, J. Snaider, K. Zhu, L. Huang, *Science* **2017**, *356*, 59.

[27] F. Ceballos, H. Zhao, *Adv. Funct. Mater.* **2017**, *27*, 1604509.

[28] A. C. Jakowetz, M. L. Böhm, A. Sadhanala, S. Huettner, A. Rao, R. H. Friend, *Nat. Mater.* **2017**, *16*, 551.

[29] H. Haug, S. W. Koch, *Quantum Theory of the Optical and Electronic Properties of Semiconductors*, 5th ed., World Scientific Publishing Company, Singapore **2009**.

[30] C. Yim, V. Passi, M. C. Lemme, G. S. Duesberg, C. Ó. Coileáin, E. Pallecchi, D. Fadil, N. McEvoy, *npj 2D Mater. Appl.* **2018**, *2*, 5.

[31] F. Carbone, *Chem. Phys. Lett.* **2010**, *496*, 291.

[32] S. Pagliara, G. Galimberti, S. Mor, M. Montagnese, G. Ferrini, M. Grandi, P. Galinetto, F. Parmigiani, *J. Am. Chem. Soc.* **2011**, *133*, 6318.

[33] M. Breusing, C. Ropers, T. Elsaesser, *Phys. Rev. Lett.* **2009**, *102*, 086809.

[34] E. A. A. Pogna, M. Marsili, D. De Fazio, S. Dal Conte, C. Manzoni, D. Sangalli, D. Yoon, A. Lombardo, A. C. Ferrari, A. Marini, G. Cerullo, D. Prezzi, *ACS Nano* **2016**, *10*, 1182.

[35] Z. Sun, A. Martinez, F. Wang, *Nat. Photonics* **2016**, *10*, 227.

[36] M. Sheik-Bahae, A. A. Said, T.-H. Wei, D. J. Hagan, E. W. Van Stryland, *IEEE J. Quantum Electron.* **1990**, *26*, 760.

[37] Z. Burshtein, P. Blau, Y. Kalisky, Y. Shimony, M. Kikta, *IEEE J. Quantum Electron.* **1998**, *34*, 292.

[38] S. Zhang, N. Dong, N. McEvoy, M. O'Brien, S. Winters, N. C. Berner, C. Yim, Y. Li, X. Zhang, Z. Chen, L. Zhang, G. S. Duesberg, J. Wang, *ACS Nano* **2015**, *9*, 7142.